

Modeling and Simulation of Integrated Photonic Interferometric Structures on SOI

Tadessem

Abstract

We design and analyze an integrated photonic circuit consisting of unbalanced Mach–Zehnder and Michelson interferometers, combined with a Bragg reflector, on a silicon-on-insulator (SOI) platform. The design process begins with waveguide mode analysis, followed by full-circuit simulations. We fabricate the devices and experimentally characterize them, comparing the measured results with simulation data. We examine the effect of optical path length imbalance on the spectral response and investigate the impact of fabrication-induced imperfections on transmission characteristics.

1 Introduction

Silicon photonics enables compact, low-loss optical components to be integrated on a chip using CMOS-compatible fabrication processes. The silicon-on-insulator (SOI) platform, characterized by the high refractive index contrast between the silicon core and the buried oxide layer, supports tightly confined optical modes, making it ideal for dense photonic integration.

In this report, we investigate the transmission spectra of integrated interferometric structures—including a Mach-Zehnder Interferometer (MZI), a Michelson Interferometer (MI), and a Bragg reflector based on sub-wavelength grating structures—all implemented using SOI strip waveguides. We perform simulations using Lumerical MODE and INTERCONNECT tools to analyze the effects of waveguide geometry, polarization (on mode profile and transmission behavior), and path imbalance on the spectral response. This work lays the foundation for the design of more advanced photonic circuits.

2 Modelling and Simulation

This study begins with the design and simulation of a **500 nm × 220 nm** silicon strip waveguide on a silicon-on-insulator (SOI) platform, optimized for operation at the telecom wavelength of **1.55 μm**. The high refractive index contrast between the silicon core ($n \approx 3.48$) and the silicon dioxide cladding ($n \approx 1.44$) ensures strong modal confinement and supports dense photonic integration. The cross-sectional schematic of the waveguide, along with the refractive index profile, is shown in **Figure 1**.

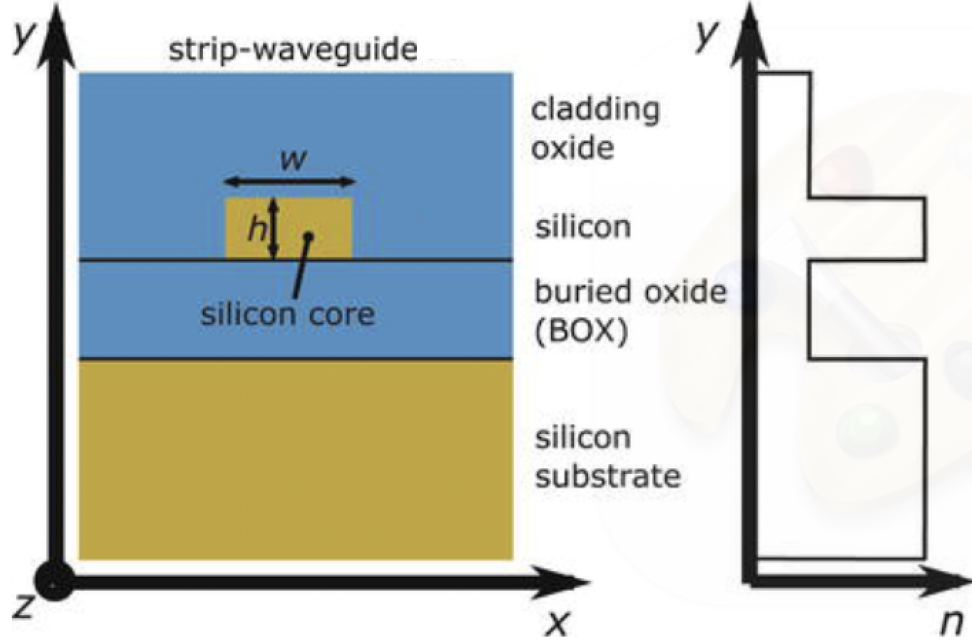


Figure 1: SOI strip Waveguide and vertical refractive index profile

2.1 Waveguide Mode Analysis

Modal analysis is carried out using *Lumerical MODE Solutions* to verify the fundamental mode profiles for both TE and TM polarizations. The computed results are shown in **Figure 2**. On the left, the TE mode is visualized via the electric field component along the x-direction (E_x), while the right illustrates the TM mode through the magnetic field component along x.

The TE mode exhibits an effective index of $n_{\text{eff}} = 2.444$, whereas the TM mode has $n_{\text{eff}} = 1.77$. As expected, the TE mode shows a noticeable discontinuity at the waveguide sidewalls, which makes it more susceptible to scattering loss due to sidewall roughness. In contrast, the TM mode is less affected by such imperfections, potentially resulting in lower propagation loss in strip waveguides.

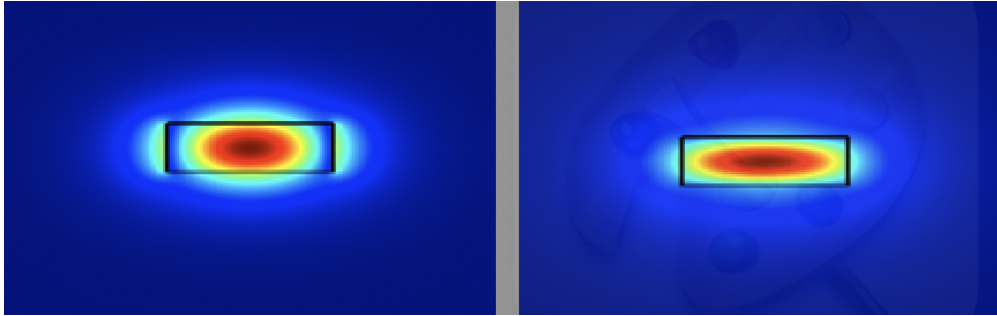


Figure 2: Fundamental mode profiles: (left) TE mode showing E_x ; (right) TM mode showing H_x .

2.2 Dispersion and Compact Modeling

After analyzing the fundamental mode profiles for both TE and TM polarizations, we proceed to investigate how the effective index varies with waveguide width. Although our design uses only the TE fundamental mode, performing a width sweep helps confirm that the chosen width of 500 nm ensures single-mode operation for the TE polarization.

We sweep the waveguide width from 200 nm to 1000 nm and plot the effective indices of the first few modes in **Figure 3**. This analysis not only confirms single-mode behavior around 500 nm, but also provides insight into multimode propagation in wider waveguides. Such knowledge is valuable when designing devices like polarization rotators, mode filters, and multi-mode couplers.

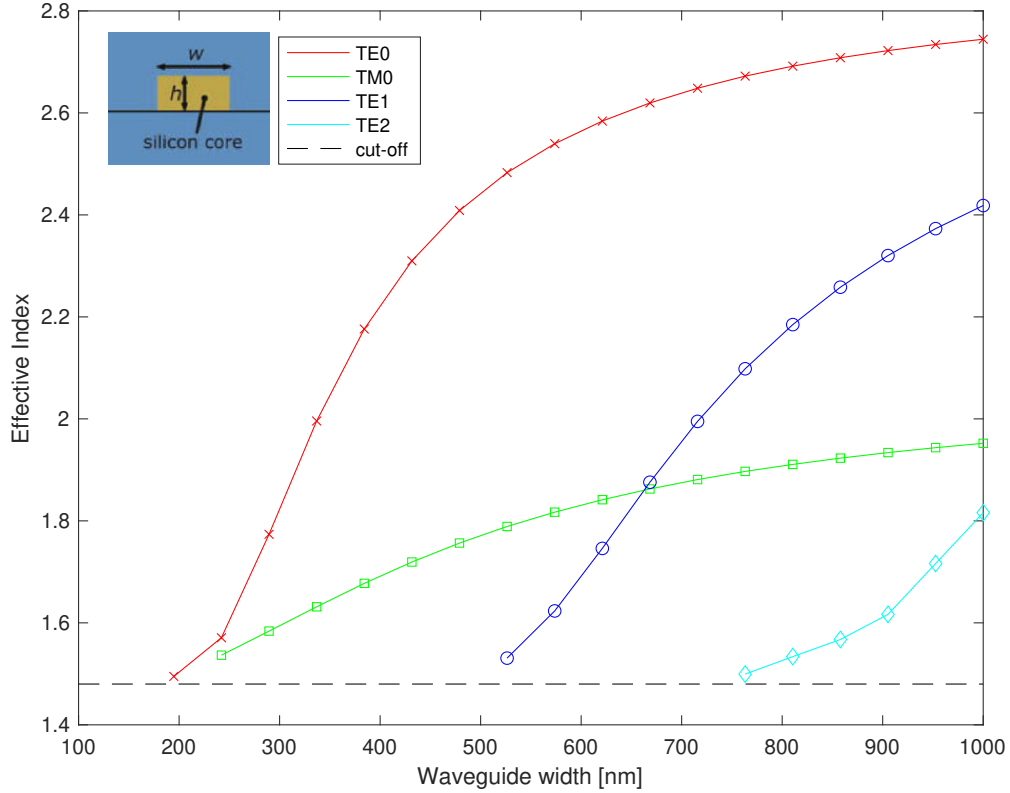


Figure 3: Effective index versus waveguide width sweep .

Next, the effective index (n_{eff}) and group index (n_g) of the TE mode are simulated over a wavelength range of 1500–1600 nm to study dispersion characteristics, which are critical in the design of interferometric circuits. The group index is calculated using:

$$n_g = n_{\text{eff}} - \lambda \frac{dn_{\text{eff}}}{d\lambda} \quad (1)$$

The results are shown in **Figure 4**, where the left panel shows the variation of effective index with wavelength, and the right panel shows the corresponding group index.

To enable fast modeling of the TE mode's dispersion behavior, a second-order polynomial is fitted to the simulated $n_{\text{eff}}(\lambda)$ data:

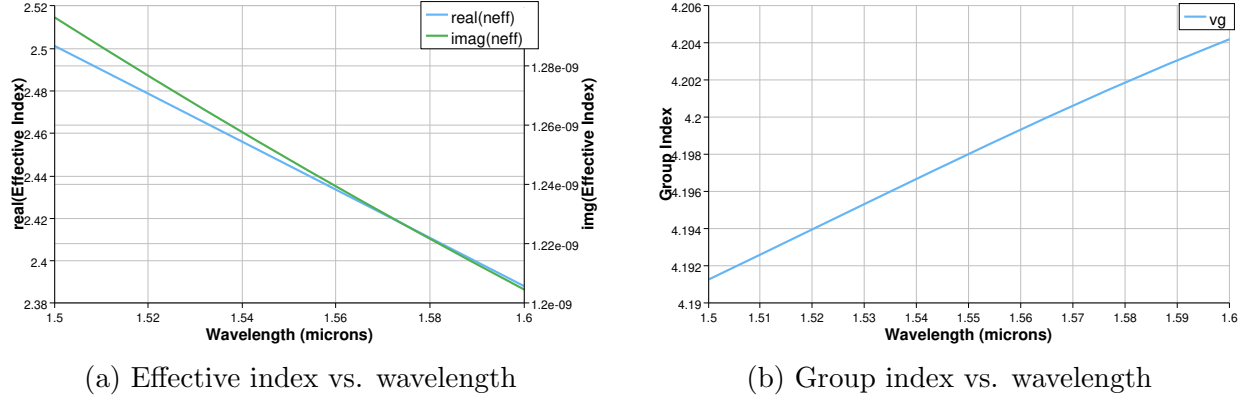


Figure 4: Dispersion characteristics of the TE mode across the 1500–1600 nm range.

$$n_{\text{eff}}(\lambda) = n_1 + n_2(\lambda - \lambda_0) + n_3(\lambda - \lambda_0)^2 \quad (2)$$

This compact model is shown in **Figure 9** and is used in subsequent device-level simulations to approximate dispersion without requiring full-field calculations. The polynomial fit coefficients are: $n_1 = 2.445$, $n_2 = -1.130$, and $n_3 = -0.039$.

2.3 Mach–Zehnder Interferometer (MZI)

An unbalanced Mach-Zehnder Interferometer (MZI) is modeled using the extracted waveguide parameters. The structure consists of two arms, with one arm introducing a **50 μm** path length difference, resulting in wavelength-dependent interference fringes caused by constructive and destructive interference of the optical waves propagating through each arm.

The transmission spectrum of the MZI, as a function of wavelength, is given by:

$$T_{\text{MZI}}(\lambda) = \frac{1}{2} \left[1 + \cos \left(\frac{2\pi \Delta L \cdot n_{\text{eff}}}{\lambda} \right) \right] \quad (3)$$

where $\Delta L = 50 \mu\text{m}$ is the path length difference, and n_{eff} is the effective refractive index.

The Free Spectral Range (FSR), defined as the wavelength spacing between two consecutive transmission maxima, is given by:

$$\text{FSR}_{\text{MZI}} = \frac{\lambda^2}{n_g \cdot \Delta L} \quad (4)$$

A smaller ΔL results in a larger FSR, allowing for broader spectral spacing between fringes. The Circuit diagram and the Lumerical INTERCONNECT schematic of the MZI is shown in **Figure 6**.

The simulated transmission spectra for both the balanced and unbalanced MZI configurations are presented in **Figure 7**.

The vertical offset observed in the transmission spectra reflects the insertion loss introduced by the back-to-back grating couplers.

In the case of the balanced Mach-Zehnder Interferometer (MZI), the spectrum also reveals the bandwidth profile of the vertical grating coupler. The optimal coupling occurs around

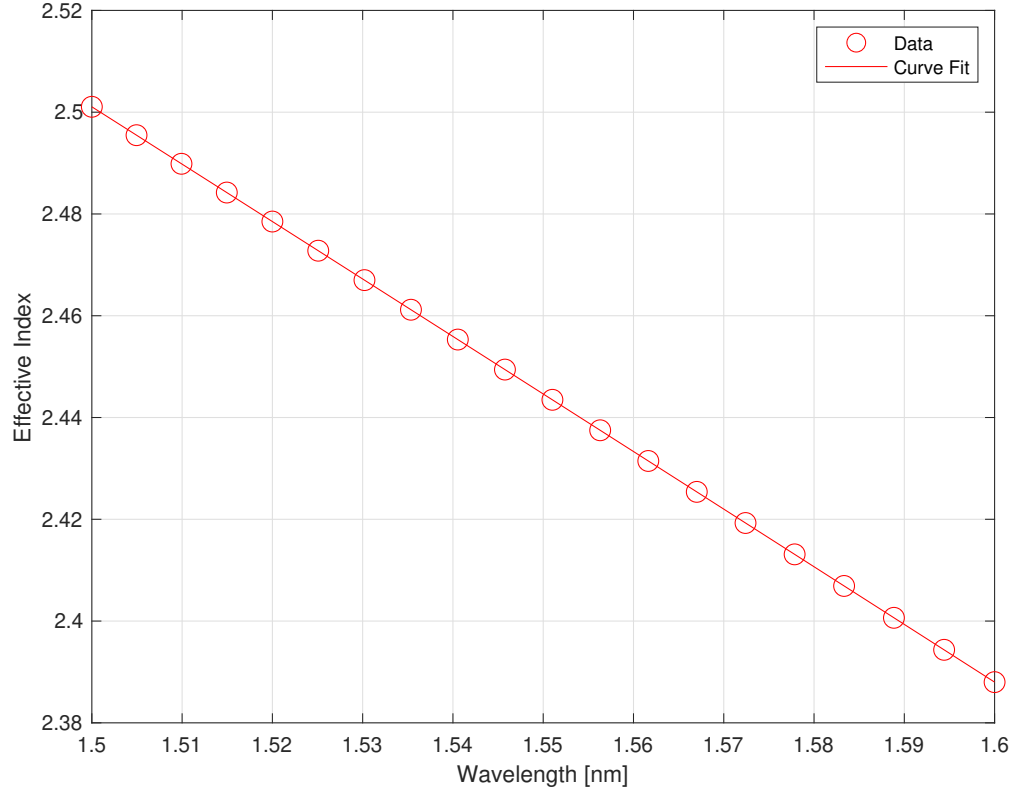
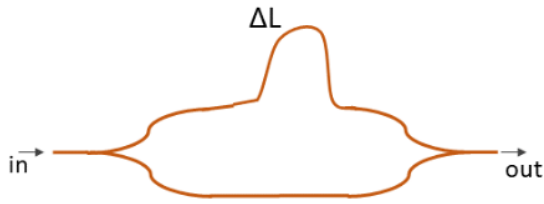
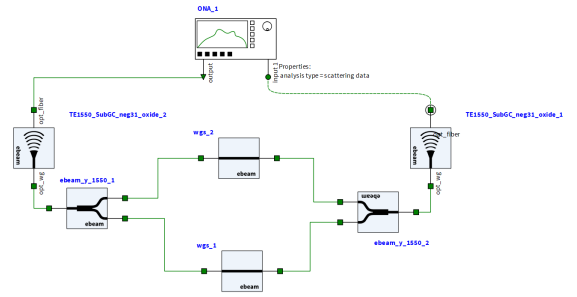


Figure 5: Second-order polynomial fit for TE mode effective index in a 500 nm-wide strip waveguide.



(a) Circuit diagram of Unbalanced MZM



(b) MZM schematic of Lumerical Interconnect

Figure 6: (a) Unbalanced MZM and (b) MZM schematic of Lumerical Interconnect.

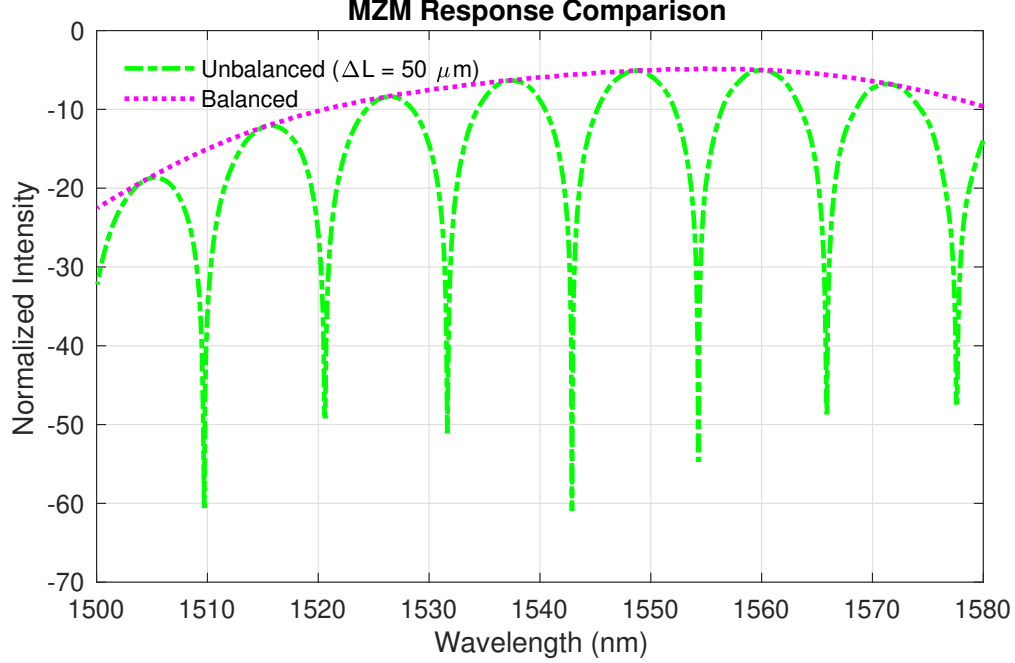


Figure 7: Transmission spectrum of MZI.

1550 nm, which corresponds to the grating's peak efficiency. As the wavelength deviates from 1550 nm on either side, increased insertion loss is observed, attributed to the limited bandwidth of the grating.

Another key observation is the Free Spectral Range (FSR) of the unbalanced MZI with a path length difference of $\Delta L = 50 \mu\text{m}$. At $\lambda = 1.55 \mu\text{m}$, and using an effective group index of $n_g = 4.198$ (as extracted from Fig. 4), the FSR can be calculated using Equation (4):

$$\text{FSR} = \frac{\lambda^2}{n_g \Delta L} = \frac{(1.55 \mu\text{m})^2}{4.198 \times 50 \mu\text{m}} = 0.0114 \mu\text{m} = 11.4 \text{ nm}$$

This calculation result closely matches the simulated transmission spectrum of the MZI, where an FSR of approximately 11 nm is clearly observed, confirming the consistency between theoretical prediction and simulation.

2.4 Michelson Interferometer

The Michelson Interferometer (MI) is modeled similarly, with one arm extended by **25 μm** . The circuit schematic is shown in **Figure 8**.

In this configuration, light reflects back from the end mirrors, effectively doubling the path difference and increasing phase sensitivity. The transmission is expressed as:

$$T_{\text{MI}}(\lambda) = \frac{1}{2} \left[1 + \cos \left(\frac{4\pi L \cdot n_{\text{eff}}}{\lambda} \right) \right] \quad (5)$$

The expected FSR for the Michelson Interferometer is given by:

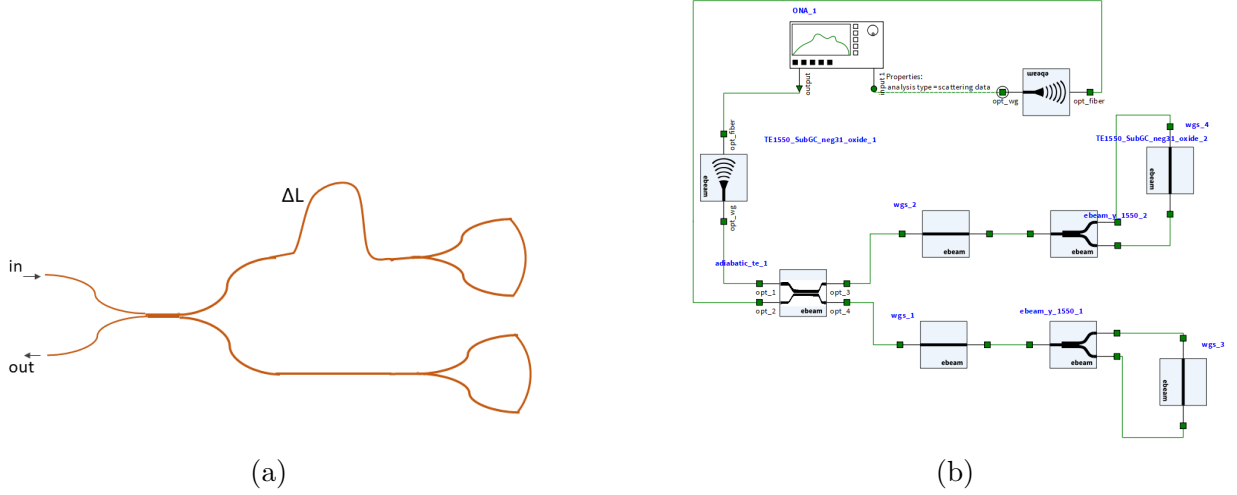


Figure 8: (a) Circuit diagram of Michelson Interferometer and (b) Michelson Interferometer schematic from Lumerical Interconnect.

$$\text{FSR}_{\text{MI}} = \frac{\lambda^2}{2 \cdot n_g \cdot \Delta L} \quad (6)$$

Here, ΔL is the physical length difference between the two arms, and the factor of 2 accounts for the round-trip propagation. Due to the doubled optical path, the Michelson Interferometer typically exhibits a smaller FSR compared to an MZI with the same physical arm difference. The measured transmission spectrum of the $25 \mu\text{m}$ unbalanced MI and the balanced version is shown in **Figure 9**, illustrating the influence of the grating coupler insertion loss.

In this case, the expected Free Spectral Range (FSR) of the transmission spectrum for $\Delta L = 25 \mu\text{m}$ is theoretically the same as that of the MZI with $\Delta L = 50 \mu\text{m}$, due to the round-trip nature of the Michelson interferometer. However, the observed FSR in the simulation is approximately 21 nm, which appears inconsistent at first.

This discrepancy arises from the circuit layout: in the current design, the path difference ΔL is implemented in the Y-branch mirror section. Ideally, the delay line should be placed immediately after the 2x2 coupler like the circuit in Fig 8(a), so that the optical signal encounters it twice — once during the forward path and once during the reflection. However, when the delay is placed in the mirror arm, the light passes through it only once.

Referring to Equation (6), if we substitute $2\Delta L = 25 \mu\text{m}$ (i.e., an effective one-way delay of $12.5 \mu\text{m}$), the FSR is calculated as:

$$\text{FSR} = \frac{(1.55 \mu\text{m})^2}{4.198 \times 25 \mu\text{m}} = 0.0228 \mu\text{m} = 22.8 \text{ nm}$$

This value closely matches the FSR observed in the simulated transmission spectrum, confirming the impact of the delay line implemented in the mirror section of the Michelson interferometer.

An additional and somewhat unexpected observation can be made from Fig. 9. Under balanced conditions, the Michelson interferometer exhibits a noticeably higher insertion loss

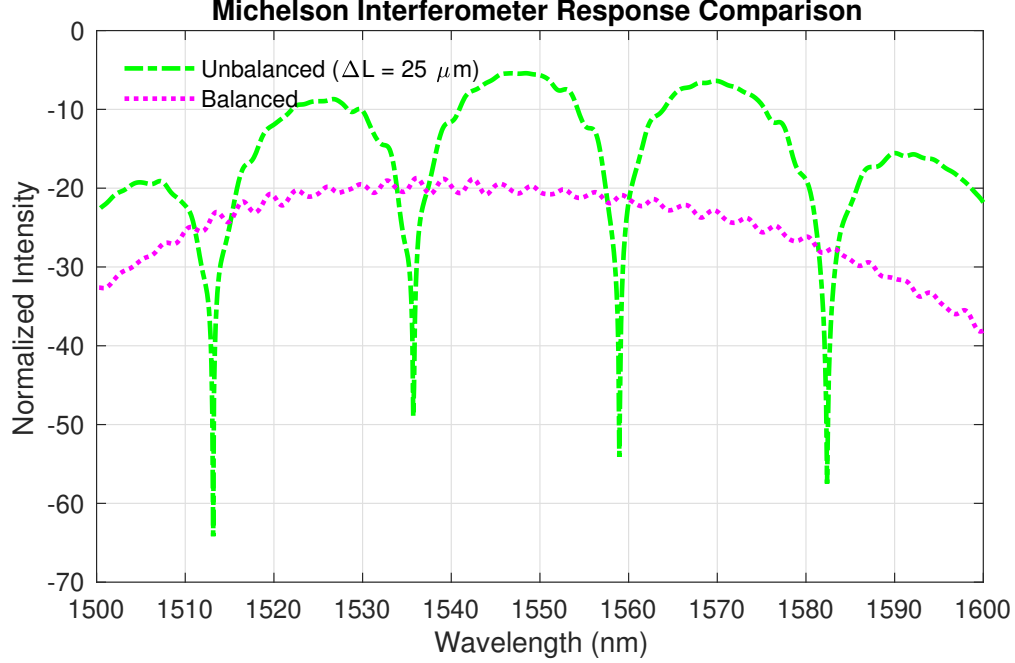


Figure 9: Transmission spectrum of Michelson Interferometer

compared to the unbalanced configuration. This outcome is counterintuitive, as one would typically expect both configurations to exhibit comparable insertion loss. The underlying reason for this increased loss in the balanced case is not fully understood at this time.

2.5 Bragg Reflector

A Bragg reflector is implemented by periodically modulating the refractive index along the waveguide. The Bragg condition is given by:

$$\lambda_B = 2n_{\text{eff}}\Lambda \quad (7)$$

The Bragg waveguide used from the **SIPIEC** library has a grating period of $\Lambda = 318$ nm and a corrugation amplitude (width modulation) of 100 nm, defined as $W_{\text{max}} - W_{\text{min}}$. The total length of the grating structure is $95 \mu\text{m}$, which corresponds to approximately 299 periods.

For a corrugated waveguide, the effective index can be approximated by averaging the effective indices of the wide and narrow segments over one grating period:

$$n_{\text{eff}}^{\text{avg}} = \frac{w_{\text{high}}}{\Lambda} n_{\text{high}} + \frac{w_{\text{low}}}{\Lambda} n_{\text{low}} \quad (8)$$

Where:

- w_{high} , w_{low} are the lengths of the wide and narrow segments along the propagation direction, respectively.
- n_{high} , n_{low} are the corresponding effective indices of those segments, typically obtained from straight waveguide simulations.

- $\Lambda = w_{\text{high}} + w_{\text{low}}$ is the period of the grating.

we have a 50% duty cycle, $w_{\text{high}} = w_{\text{low}} = 159$ nm. The wide and narrow waveguide widths are 550 nm and 450 nm, respectively. Referring to Fig. 3 for modal analysis, we find $n_{\text{high}} = 2.5$ and $n_{\text{low}} = 2.35$. Using the averaging formula:

$$n_{\text{eff}}^{\text{avg}} = \left(\frac{159}{318} \right) \cdot 2.5 + \left(\frac{159}{318} \right) \cdot 2.35 = 2.425$$

Substituting into the Bragg condition:

$$\lambda_B = 2 \cdot 2.425 \cdot 318 \text{ nm} = 1542 \text{ nm}$$

The circuit diagram and the numerical INTERCONNECT schematic of the Bragg reflector is shown in Fig 10.

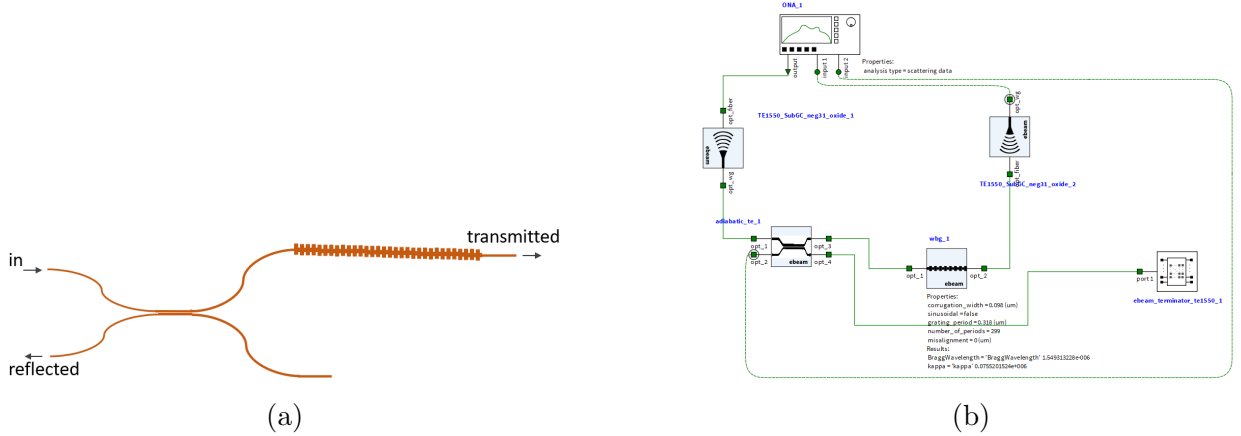


Figure 10: (a) Circuit diagram of the Bragg reflector and (b) Bragg reflector schematic implemented in Lumerical INTERCONNECT.

The corresponding transmission and reflection spectrum is presented in **Figure 11**.

The spectrum confirms that the Bragg reflector functions as intended, reflecting a narrow band of wavelengths around the Bragg wavelength while transmitting others. This behavior effectively forms a band-stop (in transmission) and band-pass (in reflection) filter. The observed Bragg wavelength is approximately 1549 nm, which has a shift of 7nm from the calculated value of 1542 nm.

3 Fabrication and Experimental Data Comparison

The photonic devices were fabricated by **Applied Nanotools Inc.** using their NanoSOI platform. The fabrication process was based on 220 nm silicon-on-insulator (SOI) substrates. Device patterns were defined using 100 keV electron beam lithography on hydrogen silsesquioxane (HSQ) resist with a JEOL JBX-8100FS system. After development, the structures were transferred into the silicon layer via chlorine-based inductively coupled plasma

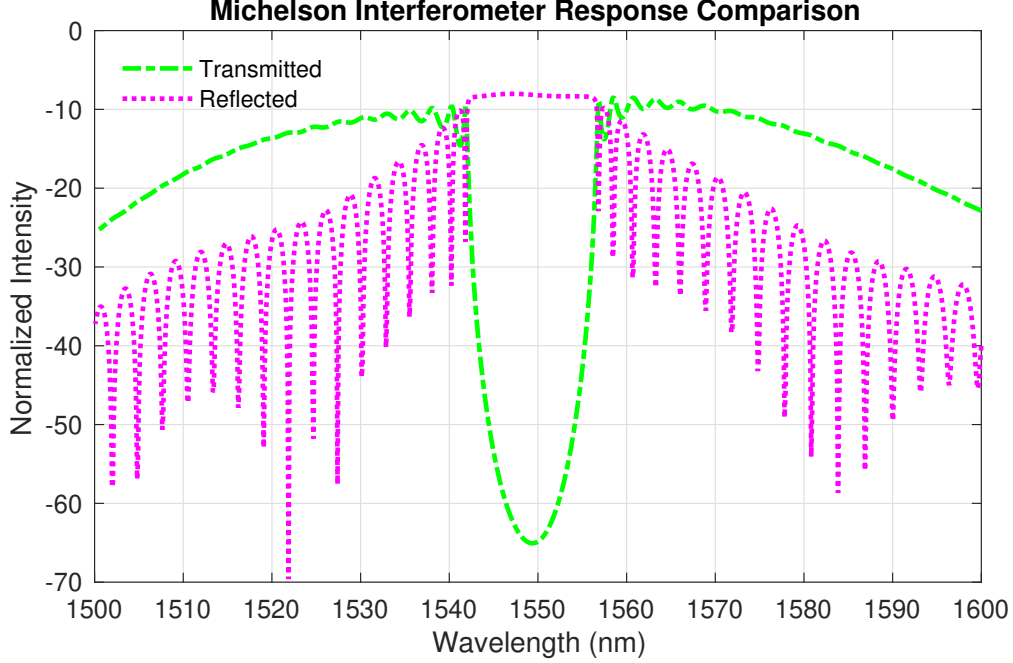


Figure 11: Transmission and reflection spectrum of the Bragg reflector.

reactive ion etching (ICP-RIE). A 2.2 μm oxide cladding was subsequently deposited using plasma-enhanced chemical vapor deposition (PECVD). The devices were inspected and verified at multiple stages to ensure pattern fidelity and process consistency.

This section compares the simulated results with experimental measurements for the fabricated Mach-Zehnder Interferometer (MZI), Michelson Interferometer, and Bragg Reflector. The aim is to validate the simulation models and assess the performance impact of fabrication-related variations.

Mach-Zehnder Interferometer (MZI)

To compare measurements with simulations, a merged transmission plot is used. Figure 12 shows the measured and simulated transmission spectra of the MZI with a 50 μm path length difference.

A noticeable observation is that the insertion loss in the experimental result is higher than that in the simulation. This is primarily due to the idealized coupling conditions assumed in simulation, in contrast to real-world imperfections of vertical grating couplers (GCs). Nevertheless, the experimental data shows good agreement with the simulation in terms of the free spectral range (FSR). The measured FSR for the unbalanced MZI with $\Delta L = 50 \mu\text{m}$ is approximately 11 nm, closely matching the simulated value of 11.4 nm.

Discrepancies are observed in the fringe extinction ratio and a shift in the resonance peaks, which may be attributed to fabrication imperfections such as waveguide width and height variations, sidewall roughness, imbalanced splitters, or phase mismatch between the arms. Additionally, the grating couplers exhibit suboptimal performance in the 1500–1530 nm range. This may be due to errors in the GC component selection from the SiEPIC library or non-ideal incidence angle during the measurement.

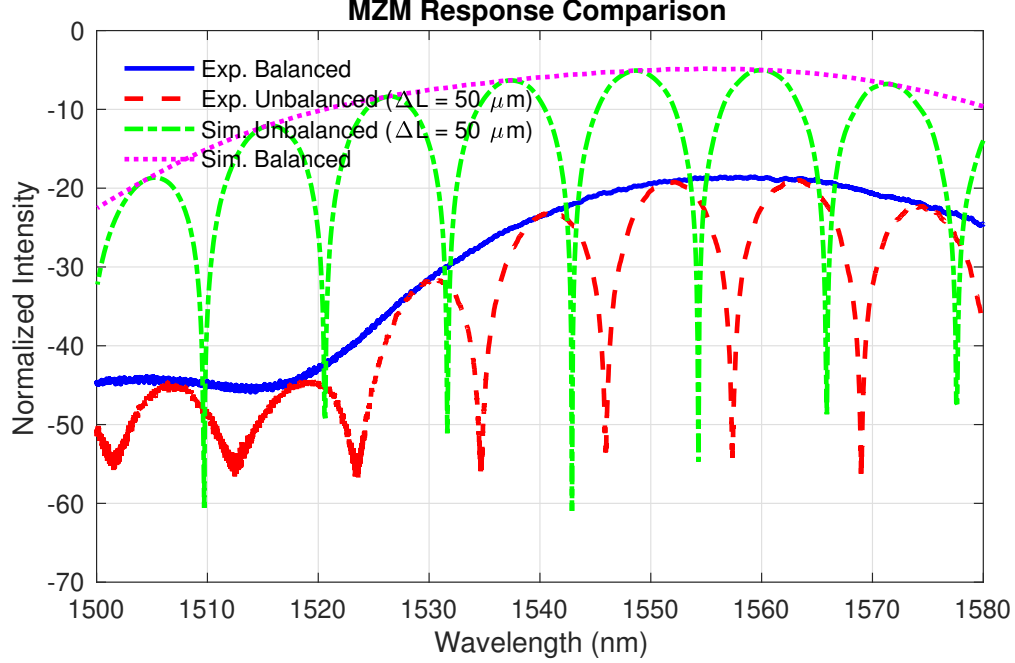


Figure 12: Transmission spectrum of MZI: simulation vs. experimental measurement.

Michelson Interferometer

For the Michelson configuration, the experimental spectrum also shows good agreement with the simulation. Figure 17 displays both the simulated and measured transmission spectra.

As the same grating couplers are used for all devices, the observed insertion loss trend and performance dip between 1500–1530 nm persists here as well. Beyond that, the measured data aligns well with the simulation except the shift in the resonance peaks.

In this design, a $\Delta L = 25 \mu\text{m}$ path difference is applied in the mirror section of the circuit, which means the light only encounters the delay once instead of making a round trip as originally intended. This results in an FSR of approximately 22 nm, which matches the theoretical expectation and confirms the modeling analysis.

Interestingly, the insertion loss for the *balanced* Michelson interferometer is observed to be slightly higher than that of the unbalanced configuration. While the difference is less pronounced than in the simulations, the experimental results still exhibit this trend. Additionally, minor ripples are present in the spectrum, which may be attributed to internal reflections at the Y-branch or coupler interfaces within the circuit, potentially forming a weak Fabry–Pérot cavity.

Bragg Reflector

The Bragg reflector also shows excellent agreement between simulation and experimental results. Figure 18 presents the transmission and reflection spectra for both cases.

The measured Bragg wavelength is centered around 1549 nm, which matches the simulation precisely. Apart from the grating coupler performance issue discussed earlier, the experimental results are highly consistent with the simulation.

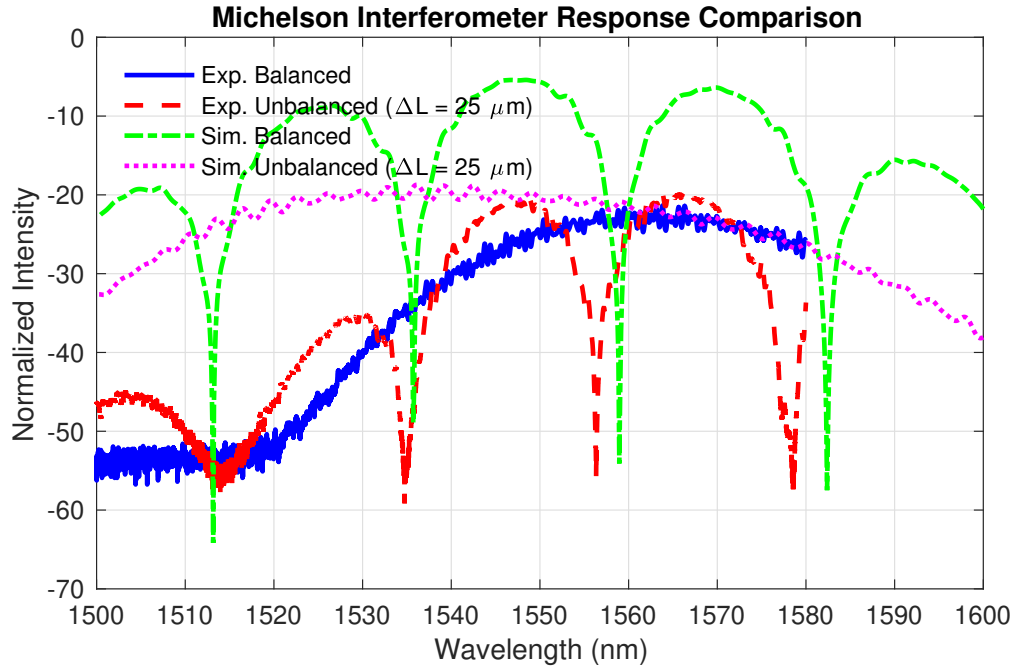


Figure 13: Transmission spectrum of Michelson Interferometer: simulation vs. measurement.

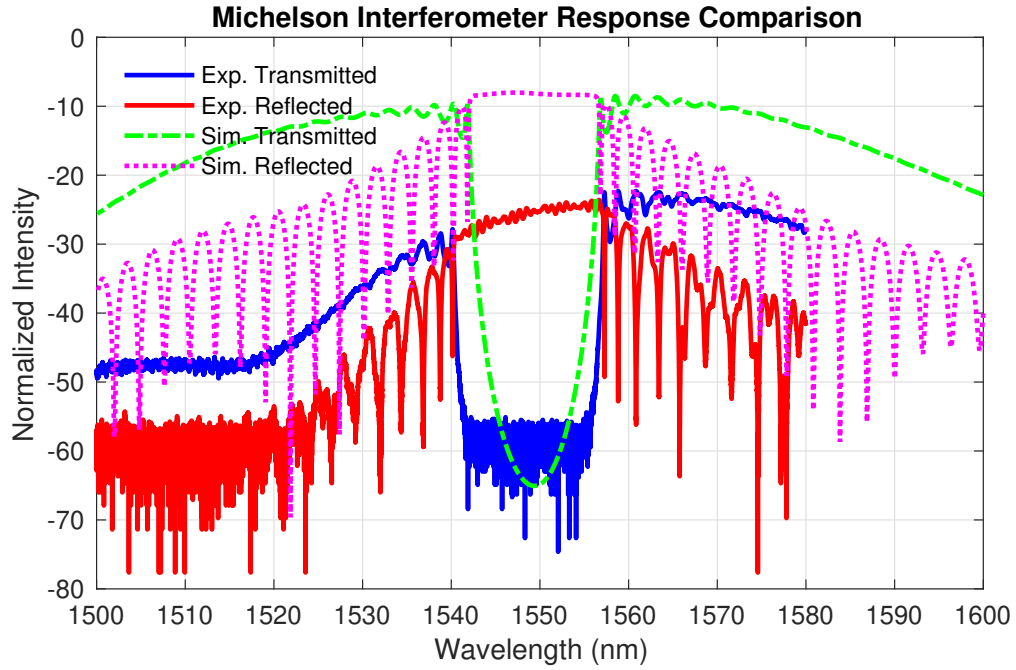


Figure 14: Transmission and reflection spectrum of Bragg reflector: simulation vs. measurement.

Both the stopband and passband characteristics are well-preserved.

4 Analysis and Conclusion

Mach-Zehnder Interferometer (MZI): To isolate the intrinsic characteristics of the device, the grating coupler (GC)-induced bandwidth limitations and insertion loss were removed through baseline correction. The resulting experimental and simulated spectra of the unbalanced Mach-Zehnder modulator (MZM), shown in Fig. 15, exhibit excellent agreement in terms of free spectral range (FSR), with both yielding approximately 11 nm. The primary discrepancy is a wavelength shift between the spectra, which is primarily attributed to fabrication imperfections.

To explore this further, a compact model was developed to account for variations in waveguide cross-section and height. A corner analysis, shown in Fig. 16, was performed under nominal and extreme waveguide crosssections. This revealed a wavelength variation of up to 4 nm among different waveguide geometries. The observed shift in Fig. 15 falls within this range, confirming that fabrication-induced deviations in waveguide dimensions are the most likely cause.

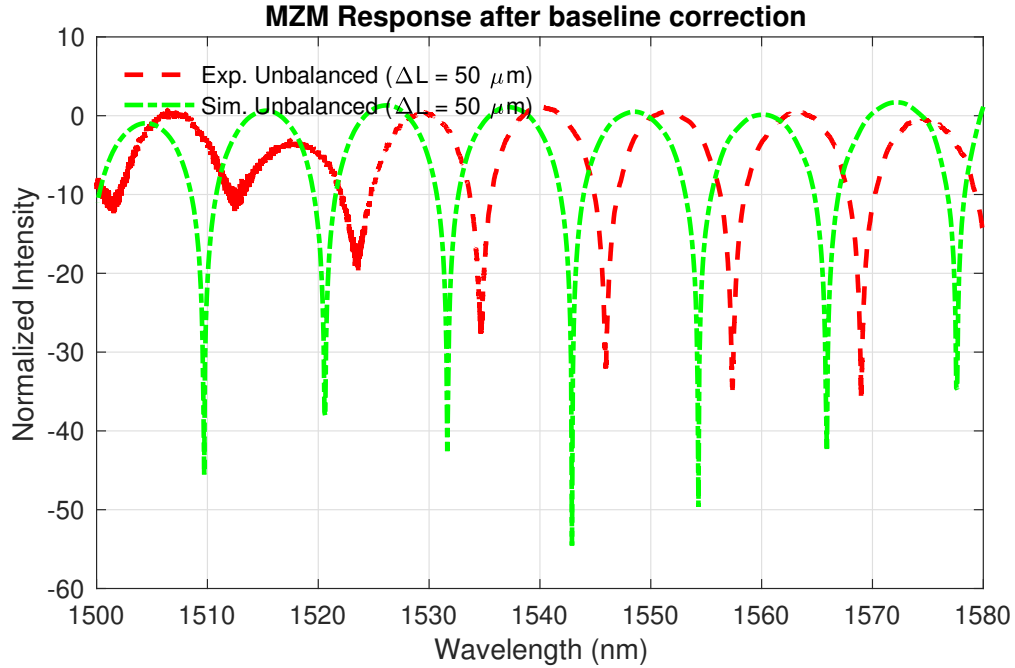


Figure 15: Transmission spectrum of unbalanced MZI after baseline correction.

Michelson Interferometer: A similar baseline correction was applied to the simulated and measured spectra of the Michelson interferometer with a $25 \mu\text{m}$ path length difference. The corrected results, shown in Fig. 17, confirm a consistent FSR between simulation and experiment. The wavelength offset observed is again attributed to fabrication-induced variation and remains within the bounds predicted by the corner analysis of the MZI.

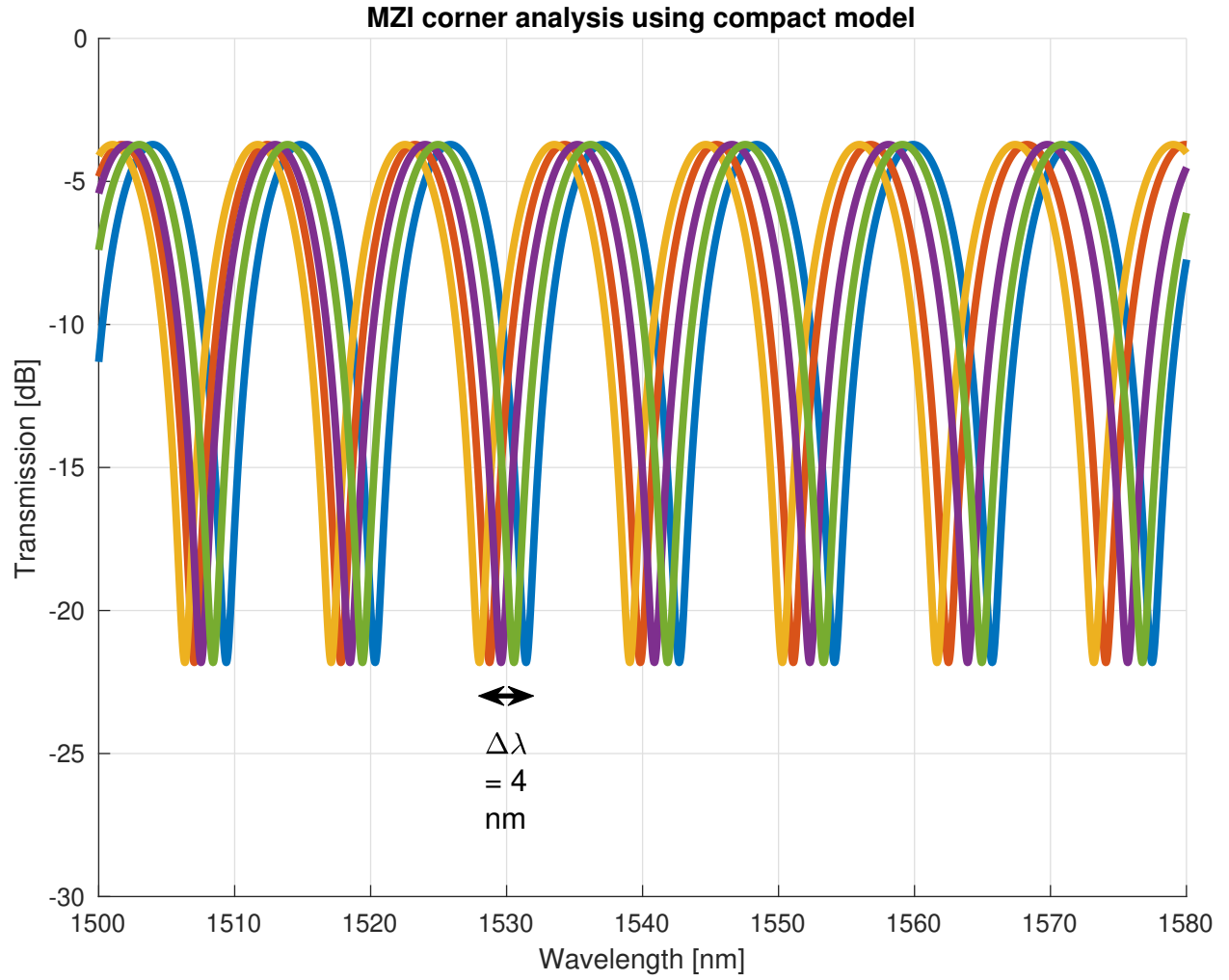


Figure 16: Corner analysis of unbalanced MZI ($\Delta L = 50 \mu\text{m}$) showing transmission spectra under varying waveguide crosssection.

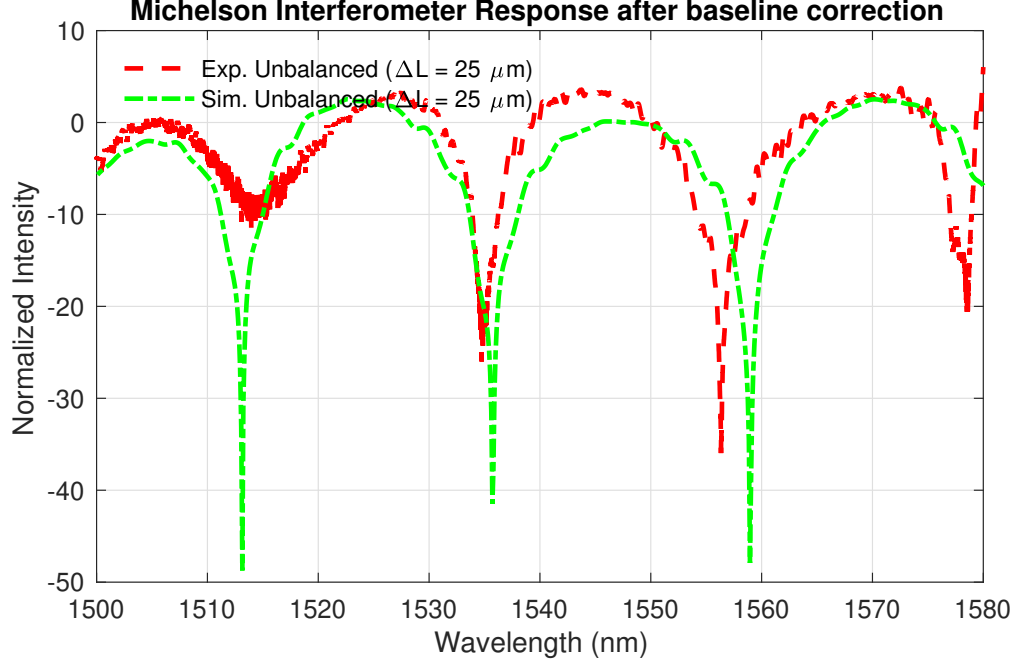


Figure 17: Transmission spectrum of unbalanced Michelson Interferometer after baseline correction.

Bragg Reflector: Baseline correction was also applied to the Bragg reflector to mitigate the effects of sub-optimal GC performance and insertion loss. The resulting transmission and reflection spectra are shown in Fig. 18. While the designed Bragg wavelength was $\lambda_B = 1542$ nm, the measured peak occurs at $\lambda_B = 1548.5$ nm, indicating a shift of 6.5 nm. This deviation, slightly larger than those observed in the interferometers, is again attributed to fabrication tolerances.

The design, simulation, and experimental validation of integrated photonic interferometric structures on the SOI platform demonstrated strong alignment between theoretical predictions and measured results. Three fundamental optical components—an unbalanced Mach-Zehnder Interferometer (MZI), a Michelson Interferometer (MI), and a Bragg reflector were analyzed using mode solving and full-circuit simulations in Lumerical INTERCONNECT.

For the unbalanced MZI, the simulated and measured FSRs matched closely. Minor spectral shifts and extinction ratio discrepancies were consistent with fabrication-induced variations, as confirmed by corner analysis.

In the Michelson interferometer, accounting for round-trip propagation in the delay arm was essential for accurate FSR prediction. This adjustment reconciled differences between expected and observed results. A notable finding was the unexpectedly high insertion loss under balanced conditions, potentially due to internal reflections or waveguide junction losses, which merits further study.

The Bragg reflector exhibited the expected band-stop behavior in transmission and band-pass behavior in reflection. However, the observed Bragg wavelength shift, though slightly larger than predicted, is consistent with fabrication errors.

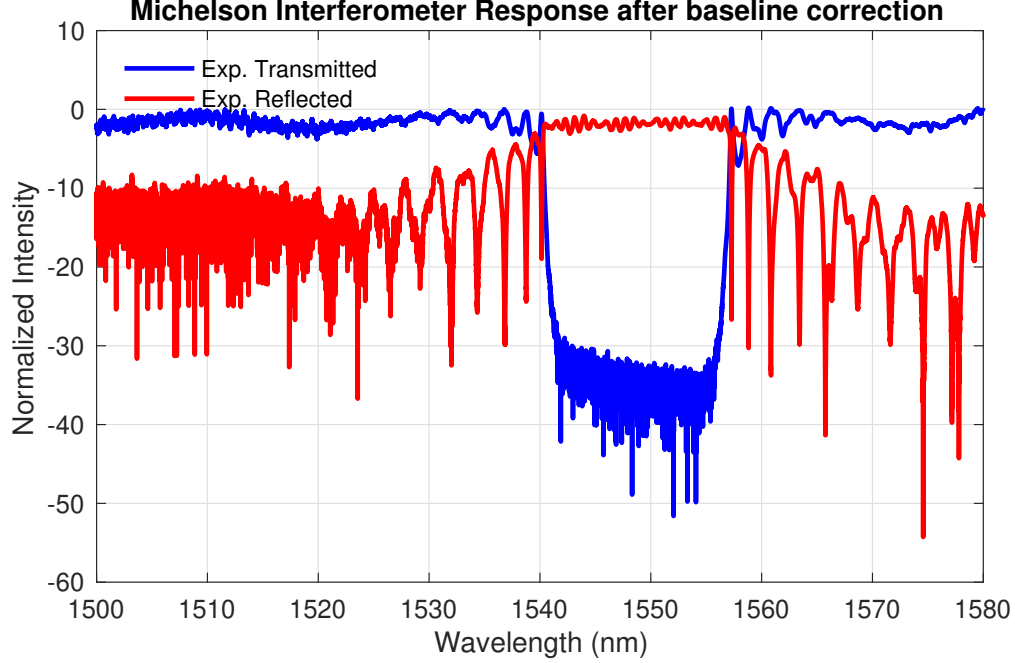


Figure 18: Transmission and reflection spectrum of Bragg reflector: after baseline correction.

Overall, this work validates the predictive accuracy of compact modeling and simulation when fabrication variability is considered. It underscores the importance of component-level modeling, including couplers and delay segments, in accurately simulating full photonic circuits. These findings provide a robust foundation for scalable design of more complex integrated photonic systems on the SOI platform.

5 Acknowledgments:

I/We acknowledge the edX UBCx Phot1x Silicon Photonics Design, Fabrication and Data Analysis course, which is supported by the Natural Sciences and Engineering Research Council of Canada (NSERC) Silicon Electronic-Photonic Integrated Circuits (SiEPIC) Program. The devices were fabricated by Richard Bojko at the University of Washington Washington Nanofabrication Facility, part of the National Science Foundation’s National Nanotechnology Infrastructure Network (NNIN), and Cameron Horvath at Applied Nanotools, Inc. Omid Esmaeeli performed the measurements at The University of British Columbia. We acknowledge Lumerical Solutions, Inc., Mathworks, and KLayout for the design software.

6 References

- [1] UBCx, *Phot1x: Silicon Photonics Design, Fabrication and Data Analysis*, online course material.
- [2] L. Chrostowski and M. Hochberg, *Silicon Photonics Design: From Devices to Systems*, Cambridge University Press, 2015.

[3] SiEPIC Project, SiEPIC EBeam PDK.